

Polarization-resolved Er emission in Er doped GaN bulk crystals

Cite as: J. Appl. Phys. **127**, 243107 (2020); <https://doi.org/10.1063/5.0012969>

Submitted: 06 May 2020 . Accepted: 11 June 2020 . Published Online: 26 June 2020

Z. Y. Sun , H. L. Gong, Y. Q. Yan , T. B. Smith, J. Li , J. Y. Lin , and H. X. Jiang 



View Online



Export Citation



CrossMark

ARTICLES YOU MAY BE INTERESTED IN

[Surface control and MBE growth diagram for homoepitaxy on single-crystal AlN substrates](#)
Applied Physics Letters **116**, 262102 (2020); <https://doi.org/10.1063/5.0010813>

[Direct evidence of hydrogen interaction with carbon: C-H complex in semi-insulating GaN](#)
Applied Physics Letters **116**, 262101 (2020); <https://doi.org/10.1063/5.0010757>

[Room-temperature operation of c-plane GaN vertical cavity surface emitting laser on conductive nanoporous distributed Bragg reflector](#)
Applied Physics Letters **117**, 011101 (2020); <https://doi.org/10.1063/5.0012281>

Lock-in Amplifiers
up to 600 MHz



Watch



Polarization-resolved Er emission in Er doped GaN bulk crystals

Cite as: J. Appl. Phys. 127, 243107 (2020); doi: 10.1063/5.0012969

Submitted: 6 May 2020 · Accepted: 11 June 2020 ·

Published Online: 26 June 2020



View Online



Export Citation



CrossMark

Z. Y. Sun,  H. L. Gong, Y. Q. Yan,  T. B. Smith, J. Li,  J. Y. Lin,  and H. X. Jiang^{a)} 

AFFILIATIONS

Department of Electrical and Computer Engineering, Texas Tech University, Lubbock, Texas 79409, USA

^{a)}Author to whom correspondence should be addressed: hx.jiang@ttu.edu

ABSTRACT

Erbium-doped GaN (Er:GaN) quasi-bulk crystals are emerging as a promising novel gain medium for high energy lasers emitting at the retina-safe wavelength window of 1.5 μm . We report the polarization-resolved photoluminescence (PL) emission spectroscopy studies, which revealed that the pumping efficiency with the excitation polarization parallel to the c -axis of GaN ($E \parallel \vec{c}$) is significantly higher than that with the excitation polarization perpendicular to the c -axis of GaN ($E \perp \vec{c}$). This phenomenon is a direct consequence of the inherent polar wurtzite GaN lattice, giving rise to a net local field, surrounding each Er ion, along the c -axis of GaN. The temperature dependent behaviors of the PL emission spectra were explained in terms of the Boltzmann population distributions among sublevels within the $^4I_{15/2}$ ground state and the $^4I_{13/2}$ first excited state of Er^{3+} in GaN, thereby providing an improved understanding regarding the origin of the dominant emission lines observed near 1.5 μm . The results suggested that the polarization field in GaN can be exploited to enhance the effective Er excitation cross section by manipulating the polarization of the excitation light source.

Published under license by AIP Publishing. <https://doi.org/10.1063/5.0012969>

I. INTRODUCTION

Erbium (Er) doped materials have attracted much attention for various applications in photonics. Doped in a solid host, with allowable intra-4f shell transitions from the first excited state ($^4I_{13/2}$) to the ground state ($^4I_{15/2}$), Er^{3+} ions can emit at the 1.5 μm wavelength window which coincides with the wavelength of the minimum optical loss in silica based optical fibers, making Er-doped materials ideal candidates for optical communication applications, such as Er-doped fiber amplifier (EDFA).^{1–4} On the other hand, Er-doped bulk materials, such as Er-doped YAG (Er:YAG) crystalline or ceramic materials, are promising for serving as novel optical gain media for solid-state high energy lasers (HELs),^{5–13} as the Er-related emission near 1.5 μm also provides an improved eye-safety and atmospheric transmission over the currently most dominant HELs based on neodymium doped YAG (Nd:YAG) emitting at 1.06 μm . The emission wavelength near 1.5 μm is considered “retina-safe” as photons in this wavelength region are strongly absorbed by the surface of the eye and consequently, the maximum permissible laser exposure limit at 1.5 μm is more than 4 orders of magnitude higher than that at the wavelengths near or below 1.0 μm .^{14,15}

Gallium nitride (GaN) is among the most-studied wide bandgap semiconductors and possesses outstanding thermal, mechanical, and

optical properties. GaN based blue/green and white light emitting diodes (LEDs) and electronic devices have been widely commercialized. Due to the wide bandgap of GaN, Er-related emission lines in Er-doped GaN (Er:GaN) exhibit high thermal stability.^{16–21} Furthermore, theoretical and experimental evidence suggested that the environment created by more ionic hosts increases the emission efficiency of the intra-4f Er^{3+} transitions.^{16–21} As such, Er:GaN epilayers and quantum well structures with a typical thickness of 1 or 2 μm synthesized by molecular beam epitaxy (MBE)^{17–19} or metal organic chemical vapor deposition (MOCVD)^{20–22} have been explored for applications in chip-scale optical emitters and amplifiers for optical communication and display.

A recent development in the growth of quasi-bulk Er:GaN crystals by hydride vapor phase epitaxy (HVPE) has provided the opportunity to investigate the prospects of Er:GaN crystals as a new gain material for HELs operating at the “retina-safe” spectral region around 1.5 μm .^{23–26} One major challenge for realizing solid-state HEL systems is heat dissipation from the active gain media, which leads to the fact that the maximum attainable operating lasing power for a typical solid-state laser attached to a heat sink is, to the first order, proportional to the thermal shock parameter, κ/α^2 , where κ is the thermal conductivity and α is the thermal

expansion coefficient of the gain material.^{27,28} Therefore, given that GaN has a much higher thermal conductivity of $\kappa = 253 \text{ W/(m K)}$ and a lower thermal expansion coefficient of $\alpha \approx 3.5 \times 10^{-6} \text{ }^\circ\text{C}^{-1}$,²⁹ comparing with $\kappa = 14 \text{ W/(m K)}$ and $\alpha = 8 \times 10^{-6} \text{ }^\circ\text{C}^{-1}$ for YAG,^{30–32} HELs based on Er:GaN gain media have the potential to outperform those based on Er:YAG or Nd:YAG by a factor up to 60–90 in terms of the maximum lasing power. Moreover, GaN also possesses a small variation of refractive index (n) with temperature (T), $dn/dT = 0.7 \times 10^{-5} \text{ }^\circ\text{C}^{-1}$ at $1.5 \text{ } \mu\text{m}$,³³ which is favorable for maintaining excellent beam quality during high power lasing operation. Another advantage for Er:GaN for HEL applications is the excellent mechanical properties of GaN, such as the high fracture toughness.³⁴ Therefore, Er:GaN bulk crystals represent a highly promising candidate for the next-generation gain medium material of solid-state HELs. To enable the fabrication of the Er:GaN gain media into a variety of geometries, such as disk, rod, slab, or planar waveguide (PWG), and to facilitate heat dissipation configurations for effectively handling the high operation powers, quasi-bulk Er:GaN crystals with adequate dimensions, such as in large wafer sizes, and with a thickness of a few hundred micrometers to a few millimeters, are required.

The intra-4f shell transitions in isolated Er atoms are forbidden due to parity conservation. However, doped in a crystal host, the presence of the local fields tends to break the inversion symmetry of the Er site, thereby making those intra-4f shell transitions allowable. The Er emission efficiency not only depends on the Er doping concentration in the crystal host but is also sensitive to the local environment surrounding the Er sites. In a crystal host with a cubic structure, the local fields surrounding the Er dopants are expected to be isotropic. On the contrary, by virtue of the polar wurtzite crystal structure of GaN which lacks inversion symmetry in the c-plane, there is an internal local electric field due to spontaneous polarization in the direction along the c-axis of GaN.^{35–37} Consequently, this spontaneous polarization field could have a significant impact on the optical emission properties of Er doped in GaN.

In this work, we report the polarization-resolved photoluminescence (PL) emission spectroscopy studies carried out on Er:GaN quasi-bulk crystals at the spectral range near $1.5 \text{ } \mu\text{m}$, aimed at identifying the impact of the built-in polarization field on the efficiencies of excitation and emission of Er doped in GaN.

The temperature dependence PL measurements revealed different evolving trends with temperature for the three dominant emission lines at 1514, 1538, and 1556 nm and the results were explained in terms of the Boltzmann population distributions among different Stark sublevels within the $^4I_{15/2}$ ground state and the $^4I_{13/2}$ first excited state in Er:GaN.

II. EXPERIMENT

Quasi-bulk crystals of Er:GaN with a thickness of about 1 mm were grown by HVPE along the [0001] direction of GaN at a temperature of $1030 \text{ }^\circ\text{C}$ with a growth rate of $\sim 200 \text{ } \mu\text{m/h}$.^{23–26} Prior to the growth of the 1 mm thick Er:GaN layer, a $20\text{-}\mu\text{m}$ thick transition layer was first deposited on c-plane GaN bulk substrates, with the Er concentration changing gradually from 0 to the target doping concentration in the subsequent 1 mm Er:GaN layer. The schematic layer structure of the Er:GaN sample used in this study is shown in Fig. 1(a). The Er doping concentration is around $3 \times 10^{19} \text{ atoms/cm}^3$ as determined by secondary-ion mass spectrometry (SIMS) measurements.

The polarization-resolved PL measurement setup is schematically shown in Fig. 1(b), where two polarizers were inserted in the typical optical path of PL measurements to control the polarization. One polarizer was placed between the excitation laser source and the sample so that the polarization direction of the excitation laser, \vec{E}_{exc} , can be controlled to be parallel or perpendicular to the c-axis of the Er:GaN sample ($\vec{E}_{\text{exc}} \parallel \vec{c}$ or $\vec{E}_{\text{exc}} \perp \vec{c}$). A second polarizer was inserted before the monochromator so that the polarization direction of the collected PL emission, \vec{E}_{emi} , can be selected to be parallel or perpendicular to the c-axis ($\vec{E}_{\text{emi}} \parallel \vec{c}$ or $\vec{E}_{\text{emi}} \perp \vec{c}$). For the polarization-resolved measurements, the sample was excited using a laser diode with a lasing wavelength $\lambda_{\text{exc}} = 980 \text{ nm}$, which resonantly excites Er³⁺ ions from the ground state ($^4I_{15/2}$) manifolds to the upper state ($^4I_{11/2}$) manifolds. In addition, a frequency doubled Ti:sapphire laser ($\lambda_{\text{exc}} = 397 \text{ nm}$), which provides a near band edge excitation for GaN, was also employed as an excitation source for the temperature dependence PL experiments. The PL emission signals were collected through two focusing lenses and

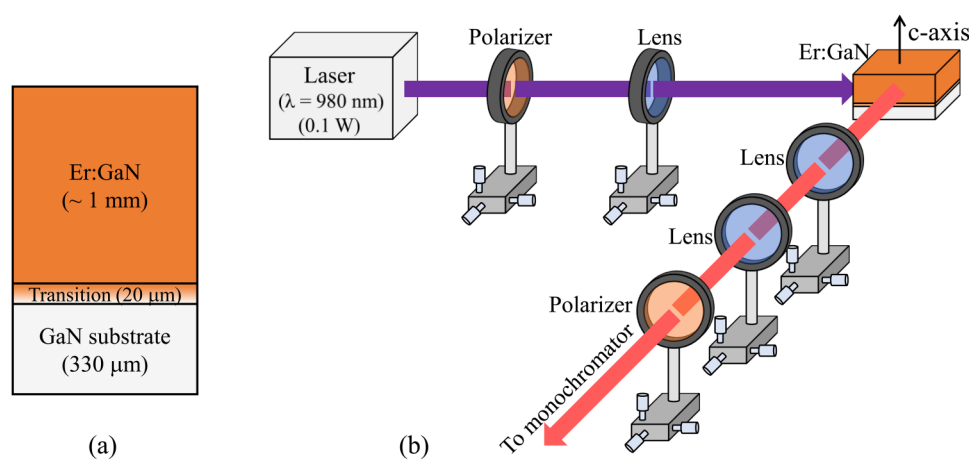


FIG. 1. Schematic diagrams of (a) structure of Er:GaN quasi-bulk crystals and (b) polarization-resolved PL spectroscopy measurement setup employed in this study.

detected by an InGaAs near-IR detector after being dispersed by a monochromator. A closed cycled helium cooled cryostat was used to vary the sample temperature from 30 to 270 K.

III. RESULTS AND DISCUSSION

Figure 2 shows the 300 K PL spectra ($\lambda_{\text{exc}} = 980 \text{ nm}$) of the Er:GaN sample under four different polarization configurations of \vec{E}_{exc} and \vec{E}_{emi} : (a) $\vec{E}_{\text{exc}} \parallel \vec{c}$ and $\vec{E}_{\text{emi}} \perp \vec{c}$, (b) $\vec{E}_{\text{exc}} \parallel \vec{c}$ and $\vec{E}_{\text{emi}} \parallel \vec{c}$, (c) $\vec{E}_{\text{exc}} \perp \vec{c}$ and $\vec{E}_{\text{emi}} \perp \vec{c}$, and (d) $\vec{E}_{\text{exc}} \perp \vec{c}$ and $\vec{E}_{\text{emi}} \parallel \vec{c}$. Three dominant emission lines at 1514, 1538, and 1556 nm resulting from the transitions between the Stark sublevels of the first excited state ($^4I_{13/2}$) and the ground state ($^4I_{15/2}$) manifolds are clearly resolved under all four polarization configurations. Moreover, the emission line at 1538 nm has the highest intensity in all four configurations. The most significant result obtained by comparing the PL spectra in Fig. 2 is that the pumping

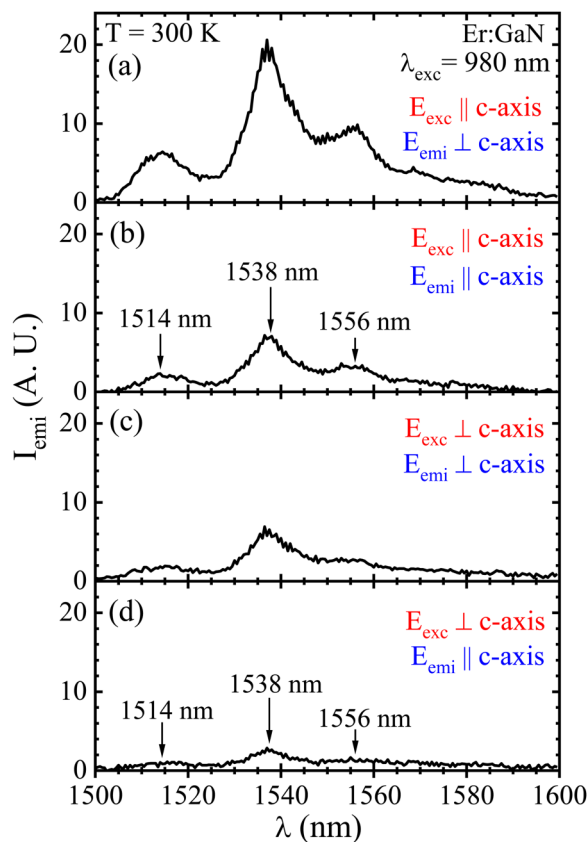


FIG. 2. PL spectra of an Er:GaN quasi-bulk crystal measured at $T = 300 \text{ K}$ for four different polarization configurations: (a) $\vec{E}_{\text{exc}} \parallel \vec{c}$ and $\vec{E}_{\text{emi}} \perp \vec{c}$, (b) $\vec{E}_{\text{exc}} \parallel \vec{c}$ and $\vec{E}_{\text{emi}} \parallel \vec{c}$, (c) $\vec{E}_{\text{exc}} \perp \vec{c}$ and $\vec{E}_{\text{emi}} \perp \vec{c}$, and (d) $\vec{E}_{\text{exc}} \perp \vec{c}$ and $\vec{E}_{\text{emi}} \parallel \vec{c}$, where \vec{E}_{exc} and \vec{E}_{emi} denote the polarization direction of the excitation laser and the collected PL emission, respectively, with $\lambda_{\text{exc}} = 980 \text{ nm}$.

configuration shown in Fig. 2(a) with $\vec{E}_{\text{exc}} \parallel \vec{c}$ and $\vec{E}_{\text{emi}} \perp \vec{c}$ provides the highest emission efficiency, whereas the configuration shown in Fig. 2(d) with $\vec{E}_{\text{exc}} \perp \vec{c}$ and $\vec{E}_{\text{emi}} \parallel \vec{c}$ provides the lowest emission intensity and the emission intensity difference between these two configurations is more than 10 times. The relative emission intensities among the three dominant emission lines remain the same for all four different configurations. Comparing the two polarization configurations of Figs. 2(a) and 2(c) with the same polarization direction for emission of $\vec{E}_{\text{emi}} \perp \vec{c}$, the results clearly revealed that the $\vec{E}_{\text{exc}} \parallel \vec{c}$ configuration or the transverse magnetic (TM) mode of excitation yields a significantly higher excitation/absorption efficiency, by a factor of almost 4 times, than the transverse electric (TE) mode of excitation ($\vec{E}_{\text{exc}} \perp \vec{c}$). The $\vec{E}_{\text{exc}} \parallel \vec{c}$ configuration has been recognized recently as the preferred excitation scheme,³⁸ but the physical origin has not been fully explored. On the other hand, for the same excitation polarization direction of $\vec{E}_{\text{exc}} \parallel \vec{c}$, comparison between the two emission polarization configurations of Figs. 2(a) and 2(b) revealed that the TE emission mode of $\vec{E}_{\text{emi}} \perp \vec{c}$ provides a much higher emission efficiency, by a factor of more than 3, than that of TM emission mode of $\vec{E}_{\text{emi}} \parallel \vec{c}$.

We believe that the result of the TM ($\vec{E}_{\text{exc}} \parallel \vec{c}$) excitation polarization mode outperforming the TE ($\vec{E}_{\text{exc}} \perp \vec{c}$) excitation polarization mode can be accounted for by the local polarization fields surrounding the Er sites in wurtzite GaN. This phenomenon is more clearly illustrated in Fig. 3, which shows that in wurtzite GaN there are four local fields acting on the Ga atom from the four nearest-neighbor nitrogen (N) atoms. Due to the wurtzite crystal-line structure, those four fields do not cancel out along the direction of the c-axis. In fact, there is a net local field acting on the Ga atom along the c-axis pointing in the $[000\bar{1}]$ direction, shown in Fig. 3(c). In Er:GaN, Er replaces Ga and hence a net field pointing in the $[000\bar{1}]$ direction is also acting on the Er atom, as a result of this polarization field. It is well known that the presence of a local electric field tends to enhance the transition probability between the first excited state ($^4I_{13/2}$) and the ground state ($^4I_{15/2}$) manifolds of Er atoms.^{17,20} For the TM ($\vec{E}_{\text{exc}} \parallel \vec{c}$) excitation configuration, the net polarization field surrounding Er atoms can be enhanced by the electric field of the excitation laser (\vec{E}_{exc}), thus, improving the transition probability, whereas for the TE ($\vec{E}_{\text{exc}} \perp \vec{c}$) excitation configuration, the enhancement of the net polarization field by the E_{exc} is not as large, therefore, not improving the transition probability as well as the TM ($\vec{E}_{\text{exc}} \parallel \vec{c}$) excitation configuration. This explains why the TM ($\vec{E}_{\text{exc}} \parallel \vec{c}$) excitation configuration provides higher quantum efficiency than that of the TE ($\vec{E}_{\text{exc}} \perp \vec{c}$) excitation configuration. On the other hand, the favored polarization configuration identified for the emission side is TE ($\vec{E}_{\text{emi}} \perp \vec{c}$). This can be explained in terms of the optical loss, considering that the PL emission generated inside the Er:GaN sample needed to propagate a distance within the material toward the exit facet, and that the TE emission mode ($\vec{E}_{\text{emi}} \perp \vec{c}$) exhibited a lower optical loss than the TM emission mode ($\vec{E}_{\text{emi}} \parallel \vec{c}$), which resulted in higher detected emission intensity for the TE emission mode than that for the TM

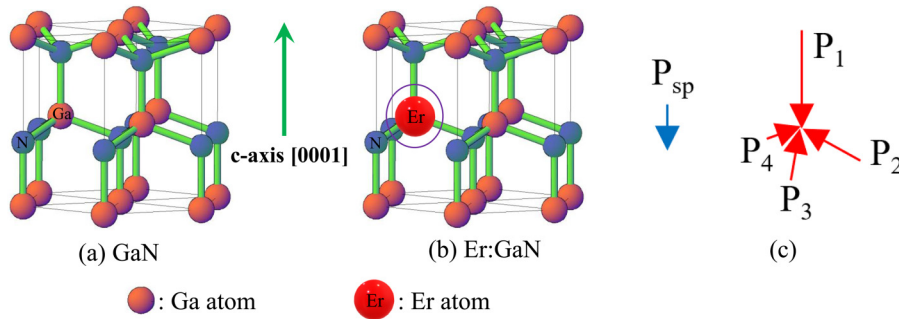


FIG. 3. Schematic representations of local configurations of (a) Ga and (b) Er atom in wurtzite GaN lattice. Different sizes of spheres (for Ga and Er) reflect the relative atomic radii of Ga and Er. (c). Schematic representation of the local fields surrounding the Er site with a net polarization field along the [0001] direction of Er:GaN.

emission mode. A higher optical loss is generally expected for the TM emission mode in most gain materials and lasers³⁹ and has also been observed recently in a GaN/Er:GaN/GaN planar waveguide structure.³⁸ The combined effects of the polarization field along the [0001] direction and lower optical loss for the TE emission mode make the polarization configuration of $E_{exc} \parallel \vec{c}$ and $\vec{E}_{emi} \perp \vec{c}$ shown in Fig. 2(a) the most preferred, while that of $\vec{E}_{exc} \perp \vec{c}$ and $\vec{E}_{emi} \parallel \vec{c}$ shown in Fig. 2(d) the least favorable.

To gain a more clear insight into the interplay among the observed three dominant emission lines at 1514, 1538, and 1556 nm and their associated energy levels, we have measured PL spectra at different temperatures from 30 to 270 K and the results are summarized in Fig. 4. It is interesting to note that the peak intensities of the 1514 and 1556 nm emission lines increase with temperature and exhibit similar temperature dependence behaviors. This suggests that these two emission lines involve the transitions from the same sublevel within the $^4I_{13/2}$ excited state manifolds or to the same sublevel within the $^4I_{15/2}$ ground state manifolds. On the other hand, the peak intensity of the 1538 nm emission line decreases with temperature. Figure 5 exhibits the evolutions of PL emission intensities with temperature for the three dominant emission lines at (a) 1514 nm, (b) 1538 nm, and (c) 1556 nm. The open blue circles are the experimental data obtained from Fig. 4. The different evolving behaviors of the emission lines at 1514 nm and 1556 nm comparing with emission line at 1538 nm can be explained in terms of the different evolving trends of the Boltzmann population factors of Stark sublevels in the first excited ($^4I_{13/2}$) and the ground ($^4I_{15/2}$) state manifolds. The transition probability between the Stark sublevel i in the $^4I_{13/2}$ excited state manifolds and the Stark sublevel j in the $^4I_{15/2}$ ground state manifolds can be described as

$$I(T) = I_0 f_{2i} (1 - f_{1j}), \quad (1)$$

where f_{2i} and f_{1j} represent the Boltzmann population distribution factors of sublevel i in the $^4I_{13/2}$ first excited state manifolds and sublevel j in the $^4I_{15/2}$ ground state manifolds, respectively, and I_0 is a proportionality constant.

The Boltzmann factors for the i th sublevel of the $^4I_{13/2}$ first excited state can be written as

$$f_{2i} = \frac{e^{-\frac{\Delta E_{2i}}{kT}}}{\sum_{n=1}^7 e^{-\frac{\Delta E_{2n}}{kT}}} \quad (i = 1, 2, \dots, 7). \quad (2)$$

The Boltzmann factors for the j th sublevel of the ground state ($^4I_{15/2}$) can be written as

$$f_{1j} = \frac{e^{-\frac{\Delta E_{1j}}{kT}}}{\sum_{n=1}^8 e^{-\frac{\Delta E_{1n}}{kT}}} \quad (j = 1, 2, \dots, 8), \quad (3)$$

where $\Delta E_{2i} = E_{2i} - E_{21}$ is the energy of the sublevel i relative to the lowest sublevel of the first excited state ($^4I_{13/2}$) manifolds, $\Delta E_{1j} = E_{1j} - E_{11}$ is the energy of the sublevel j relative to the lowest

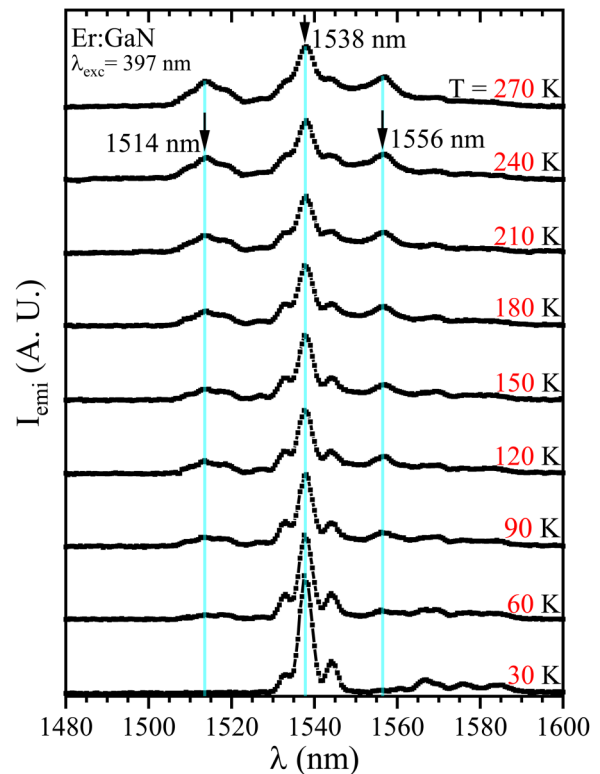


FIG. 4. Temperature dependent PL spectra of an Er:GaN quasi-bulk crystal measured between 30 and 270 K with $\lambda_{exc} = 397$ nm.

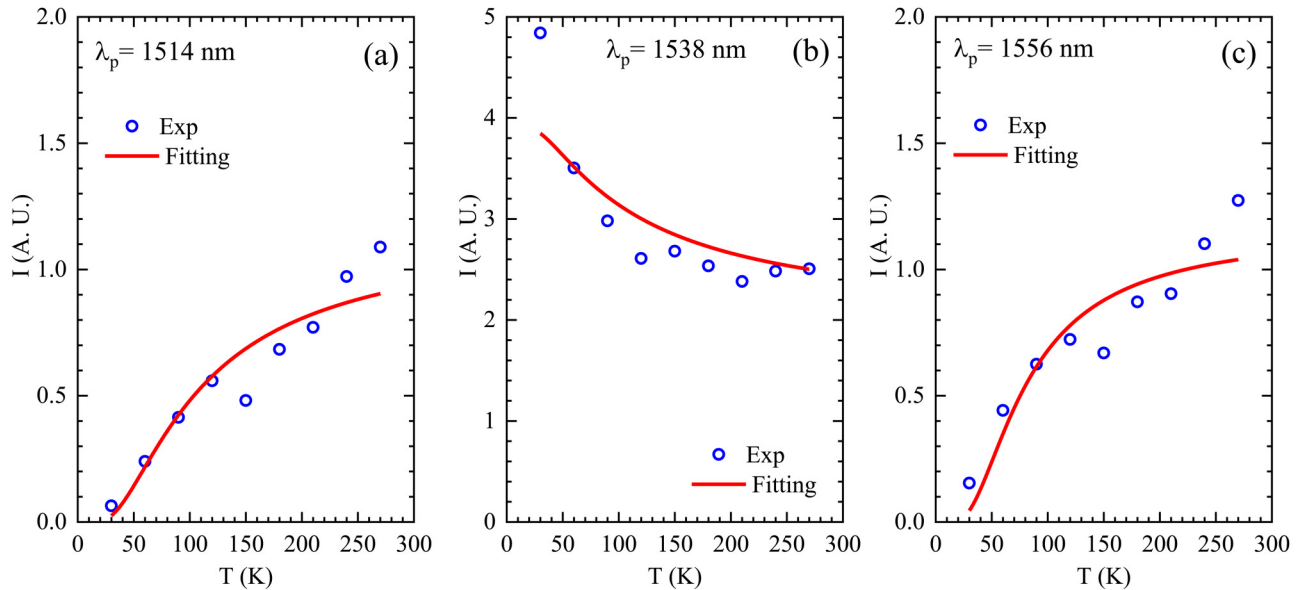


FIG. 5. Evolutions of PL peak intensities with temperature of the three dominant emission lines at (a) 1514 nm, (b) 1538 nm, and (c) 1556 nm, obtained from Fig. 4. Open blue circles are the experimental data, and the solid red curves are the least square fits of the experimental data with Eq. (4).

sublevel of the ground state ($^4I_{15/2}$) manifolds,²⁰ k is the Boltzmann constant ($k = 8.6173 \times 10^{-5} \text{ eV K}^{-1}$), and T is the temperature.

Figure 6 shows the energy level diagrams of Er:GaN in the ground ($^4I_{15/2}$) and first excited ($^4I_{13/2}$) state manifolds for (a) 30 K and (b) 300 K, constructed from the theoretically calculated energy level for each Stark sublevel from Ref. 20. Based on the PL emission peak positions, we can identify that 1514 nm emission line is due to the transitions from sublevels of $i=4$ and 5 in the $^4I_{13/2}$ first excited state manifolds to sublevels of $j=1$ and 2 in the $^4I_{15/2}$ ground state manifolds. Furthermore, the similar temperature dependent behaviors exhibited by the 1514 and 1556 nm emission lines shown in Figs. 4 and 5 suggest that the 1556 nm emission line is due to the transitions from sublevels of $i=4$ and 5 in the $^4I_{13/2}$ first excited state manifolds to sublevels of $j=7$ and 8 of the $^4I_{15/2}$ ground state manifolds. Finally, the emission line at 1538 nm can be attributed to the transitions between sublevels of $i=1$ and 2 in the $^4I_{13/2}$ first excited state manifolds to sublevels of $j=1$ and 2 of the $^4I_{15/2}$ ground state manifolds. The intensities of these three emission lines at 1514, 1538, and 1556 nm are proportional to $(f_{24} + f_{25})[(1 - f_{11}) + (1 - f_{12})]$, $(f_{21} + f_{22})[(1 - f_{11}) + (1 - f_{12})]$, and $(f_{24} + f_{25})[(1 - f_{17}) + (1 - f_{18})]$, respectively, where f_{2i} and f_{1j} are Boltzmann population factors at a certain temperature. The emission lines of 1514 and 1556 nm involve the same fourth and fifth sublevels of the $^4I_{13/2}$ first excited state and hence exhibit similar temperature dependent behaviors.

As temperature increases, the Boltzmann populations in the higher sublevels of $i=4$ and 5 in the $^4I_{13/2}$ first excited state manifolds increase, which explains why the intensities of the 1514 and 1556 nm emission lines increase with increasing temperature. Meanwhile, the Boltzmann populations in the lowest sublevels of $i=1$ and 2 of the $^4I_{13/2}$ first excited state manifolds decrease with

increasing temperature. Therefore, the intensity of the 1538 nm emission line decreases with increasing temperature. As all the three main peaks at 1514, 1538, and 1556 nm involve transitions from two closely located sublevels in the $^4I_{13/2}$ first excited state and two close located sublevels in the $^4I_{15/2}$ ground state, to explain the temperature dependent behaviors of these three main emission lines, Eq. (1) should be rewritten as

$$I(T) = I_0(f_{2i} + f_{2j})[(1 - f_{1j}) + (1 - f_{1j})], \quad (4)$$

where I_0 is a constant and fitting parameter and f_{2i} and f_{1j} are Boltzmann population factors as functions of temperature, which are involved in the transitions for certain emission lines in the temperature dependence PL spectra. To account for the temperature dependent behaviors, the peak intensities of the three main emission lines at 1514, 1538, and 1556 nm have been fitted with Eq. (4) with the corresponding Boltzmann population factors, shown as the solid curves in Fig. 5. As shown in Fig. 5, the fitted curves follow the same trends as the experimental data, indicating the different evolving behaviors with temperature between the three dominant emission lines at 1514 nm, 1556 nm, and the 1538 nm are mainly due to the redistribution of the Boltzmann populations at different temperatures among the Stark sublevels involved in the transitions of these three emission lines.

IV. SUMMARY

In summary, polarization-resolved and temperature dependent PL emission properties of Er:GaN quasi-bulk crystals grown by HVPE have been studied in the retina-safe spectral window of 1.5 μm . Our results indicate that the pumping efficiency for the TM

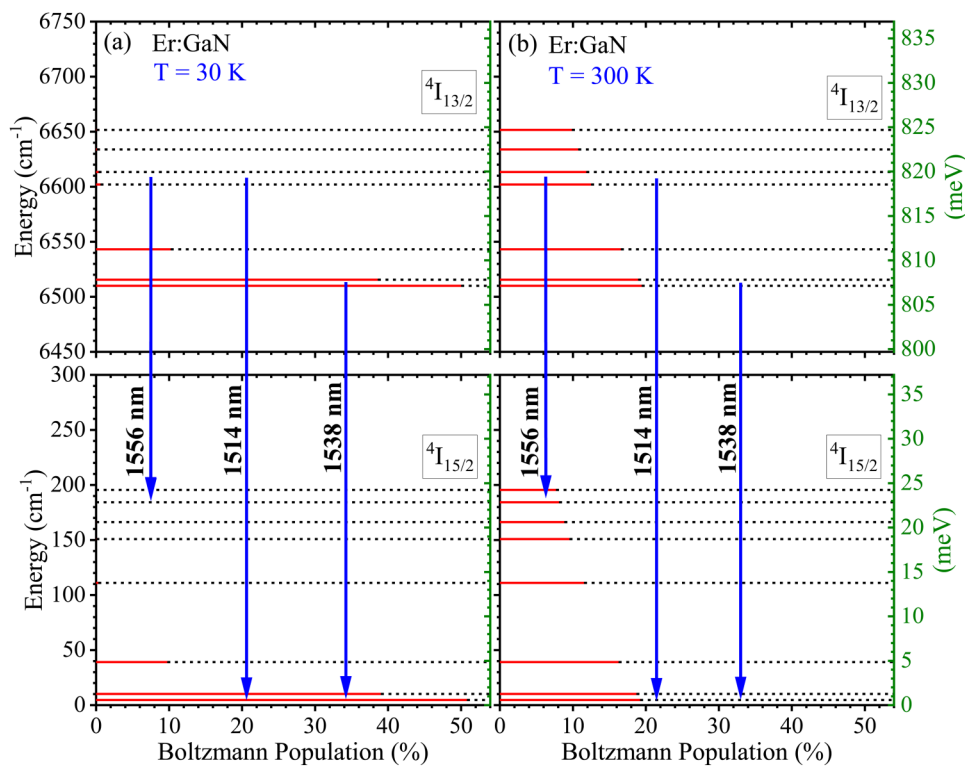


FIG. 6. Energy level diagram of Er^{3+} in the (${}^4I_{13/2}$) first excited state manifolds and (${}^4I_{15/2}$) ground state manifolds in Er:GaN at (a) $T = 30$ K and (b) $T = 300$ K. The vertical bold solid arrow lines indicate the transitions of the dominant emission lines at 1514, 1538, and 1556 nm. The Boltzmann population factors for each energy sublevels are indicated by the red horizontal solid lines.

excitation polarization mode ($\vec{E}_{\text{exc}} \parallel \vec{c}$) is much higher than that of TE excitation polarization mode ($\vec{E}_{\text{exc}} \perp \vec{c}$). This is a direct consequence of the polar wurtzite structure of GaN, giving rise to local polarization fields surrounding the Er site with a net field pointing to the opposite direction of the c -axis. The results thus suggested that the effective Er excitation cross section also depends on the polarization orientation of the excitation light source. The temperature dependent behaviors of the PL emission spectra obtained from 30 to 270 K can be explained in terms of the Boltzmann population distributions among different Stark sublevels within the ${}^4I_{15/2}$ ground state and the ${}^4I_{13/2}$ first excited state manifolds in Er:GaN, which provided an improved insight into the transition mechanisms of the three dominant emission lines near $1.5 \mu\text{m}$. More importantly, these results revealed that the inherent material property of the polarization field in GaN can be exploited and it provided important information regarding how to effectively pump Er:GaN for realizing retina-safe HELs. More specifically, by utilizing the effects of polarization field along the c -axis and the minimum optical loss in the direction of perpendicular to the c -axis, the identified optimal optical pumping configuration for solid-state HELs based on Er:GaN consists of $\vec{E}_{\text{exc}} \parallel \vec{c}$ and $\vec{E}_{\text{emi}} \perp \vec{c}$.

ACKNOWLEDGMENTS

This work was supported by the Directed Energy—Joint Transition Office Multidisciplinary Research Initiative program and Office of Naval Research (ONR) (Grant No. N00014-17-1-2531).

H. X. Jiang and J. Y. Lin would also like to acknowledge the support of Whitacre endowed chairs by the AT & T Foundation.

DATA AVAILABILITY

The data that support the findings of this study are available from the corresponding author upon reasonable request.

REFERENCES

- W. J. Miniscalco, *J. Lightwave Technol.* **9**, 234 (1991).
- E. Desurvire, *Erbium-doped Fibre Amplifiers: Principles and Applications* (John Wiley & Sons, 1994).
- R. J. Mears, L. Reekie, I. M. Jauncey, and D. N. Payne, *Electron. Lett.* **23**, 1026 (1987).
- P. C. Becker, N. A. Olsson, and J. R. Simpson, *Erbium-Doped Fibre Amplifiers: Fundamentals and Technology* (Academic Press, 1999).
- Y. X. Fan and R. G. Schlecht, U.S. patent 4,995,046 (19 February 1991).
- N. Ter-Gabrielyan, V. Fromzel, X. Mu, H. Meissner, and M. Dubinskii, *Opt. Lett.* **38**, 2431 (2013).
- K. Spariosu, V. Leyva, R. A. Reeder, and M. J. Klotz, *IEEE J. Quantum Electron.* **42**, 182 (2006).
- J. O. White, *IEEE J. Quantum Electron.* **45**, 1213 (2009).
- M. Němec, J. Šulc, L. Indra, M. Fibrich, and H. Jelínková, *Laser Phys.* **25**, 015803 (2015).
- T. Sanamyan, *J. Opt. Soc. Am. B* **33**, D1 (2016).
- D. J. Ottaway, L. Harris, and P. J. Veitch, *Opt. Express* **24**, 15341 (2016).
- N. P. Barnes, B. M. Walsh, F. Amzajerdian, D. J. Reichle, G. E. Busch, and W. A. Carrion, *Opt. Mater. Express* **1**, 678 (2011).

- ¹³N. W. Chang, "Eye-safe Er:YAG laser for coherent remove sensing," Ph.D. thesis (The University of Adelaide, 2012).
- ¹⁴J. A. Zulich, D. J. Lund, and B. E. Stuck, *Health Phys.* **92**, 15 (2007).
- ¹⁵J. Bailey, A. Simpson, and D. Crisp, *Publ. Astron. Soc. Pac.* **119**, 228 (2007).
- ¹⁶P. N. Favennec, H. L'Halidon, M. Salvi, D. Moutonnet, and Y. Le Guillou, *Electron. Lett.* **25**, 718 (1989).
- ¹⁷R. G. Wilson, R. N. Schwartz, C. R. Abernathy, S. J. Pearton, N. Newman, M. Rubin, T. Fu, and J. M. Zavada, *Appl. Phys. Lett.* **65**, 992 (1994).
- ¹⁸R. Birkhahn, M. Garter, and A. J. Steckl, *Appl. Phys. Lett.* **74**, 2161 (1999).
- ¹⁹A. J. Steckl, J. C. Heikenfeld, D. S. Lee, M. J. Garter, C. C. Baker, Y. Q. Wang, and R. Jones, *IEEE Journal of Selected Topics in Quantum Electronics* **8**, 749 (2002).
- ²⁰M. Stachowicz, A. Kozanecki, C. G. Ma, M. G. Brik, J. Y. Lin, H. X. Jiang, and J. M. Zavada, *Opt. Mater.* **37**, 165 (2014).
- ²¹C. Ugolini, N. Nepal, J. Y. Lin, H. X. Jiang, and J. M. Zavada, *Appl. Phys. Lett.* **89**, 151903 (2006).
- ²²R. Dahal, C. Ugolini, J. Y. Lin, H. X. Jiang, and J. M. Zavada, *Appl. Phys. Lett.* **97**, 141109 (2010).
- ²³Z. Y. Sun, J. Li, W. P. Zhao, J. Y. Lin, and H. X. Jiang, *Appl. Phys. Lett.* **109**, 052101 (2016).
- ²⁴Z. Y. Sun, L. C. Tung, W. P. Zhao, J. Li, J. Y. Lin, and H. X. Jiang, *Appl. Phys. Lett.* **111**, 072109 (2017).
- ²⁵Z. Y. Sun, Y. Q. Yan, W. P. Zhao, J. Li, J. Y. Lin, and H. X. Jiang, *Appl. Phys. Lett.* **112**, 202103 (2018).
- ²⁶Z. Y. Sun, Y. Q. Yan, T. B. Smith, W. P. Zhao, J. Li, J. Y. Lin, and H. X. Jiang, *Appl. Phys. Lett.* **114**, 222105 (2019).
- ²⁷D. C. Brown, *IEEE J. Quantum Electron.* **33**, 861 (1997).
- ²⁸T. Taira, *C. R. Phys.* **8**, 138 (2007).
- ²⁹H. Shibata, Y. Waseda, H. Ohta, K. Kiyomi, K. Shimoyama, K. Fujito, H. Nagaoka, Y. Kagamitani, R. Simura, and T. Fukuda, *Mater. Trans.* **48**, 2782 (2007).
- ³⁰R. Wynne, J. L. Daneu, and T. Y. Fan, *Appl. Opt.* **38**, 3282 (1999).
- ³¹H. Furuse, R. Yasuhara, and K. Hiraga, *Opt. Mater. Express* **4**, 1794 (2014).
- ³²W. Xie, S. C. Tam, H. Yang, J. Gu, G. Zhao, Y. L. Lam, and W. Tan, *Opt. Laser Technol.* **31**, 521 (1999).
- ³³R. Hui, Y. Wan, J. Li, S. X. Jin, J. Y. Lin, and H. X. Jiang, *IEEE J. Quantum Electron.* **41**, 100 (2005).
- ³⁴Y. T. Cheng, D. J. Cai, H. Wang, J. J. Wu, X. S. Liu, G. Y. Zhang, and T. J. Yu, *Phys. Status Solidi B* **255**, 1700515 (2018).
- ³⁵E. T. Yu, X. Z. Dang, P. M. Asbeck, S. S. Lau, and G. J. Sullivan, *J. Vac. Sci. Technol. B* **17**, 1742 (1999).
- ³⁶J. M. Wagner and F. Bechstedt, *Phys. Rev. B* **66**, 115202 (2002).
- ³⁷O. Ambacher and J. Majewski, *J. Phys. Condens. Matter* **14**, 3399 (2002).
- ³⁸Y. Q. Yan, Z. Y. Sun, W. P. Zhao, J. Li, J. Y. Lin, and H. X. Jiang, *Appl. Phys. Express* **12**, 075505 (2019).
- ³⁹H. Tanaka, A. Watabe, J. Shimada, Y. Katagiri, and Y. Suzuki, U.S. patent 5,497,390 (5 March 1996).